

DESIGN OF A STRUCTURAL HEALTH MONITORING SYSTEM FOR A DAMAGE TOLERANCE FUSELAGE COMPONENT

Vincentius EWALD^{1,2}, Pedro OCHÔA¹, Roger GROVES¹, Christian BOLLER²

¹ Aerospace Non-Destructive Testing Laboratory, Faculty of Aerospace Engineering, Delft University of Technology, Delft, The Netherlands

² Chair of Non-Destructive Testing and Quality Assurance, University of Saarland, Saarbrücken, Germany
Email address: V.Ewald@tudelft.nl

ABSTRACT Most aeronautical primary structures within the civil aviation sector are designed to be damage tolerant. Cracks in the structure are allowed to initiate and propagate up to defined critical lengths in the structure and are then repaired. Damage tolerance criteria and maintenance scheduling are usually very well aligned and optimized as long as they are applied to the original design of an aircraft. However, when it comes to repairs of aging aircraft, unscheduled maintenance may be increasingly necessary and the inspection process can become increasingly costly for the operator. This is where the integration of an NDT system into a structure for automated inspection, commonly called a structural health monitoring (SHM) system becomes of interest. This paper is focused on the design of an ultrasonic guided wave SHM system for a fuselage section cut from the corner of the main entrance doorframe. This structure has been designed using a damage tolerance philosophy. The fuselage section is composed of up to five layers of aluminum and bonded stringers. A 3D model was first created by using CATIA. This digital model was then exported into commercial FEA (finite element analysis) software. In this study, the optimum mesh size and an optimum excitation frequency range were determined. Then, different sensor placement was studied in order to determine the sensor locations for the detection of damage with a minimum allowable probability.

1. Introduction

Non-Destructive Testing (NDT) techniques have increasingly been proven to enhance structural safety and durability in civil and military aviation. As the deployment of autonomous structures is increasing due to economic and efficiency demands, the integration of an NDT monitoring system into a structure for automated inspection [1] (commonly called structural health monitoring, SHM, system) is of interest. As referenced in [2]: “*an effective SHM system potentially minimizes the ground time for inspections, increases the availability and allows a reduction of the total maintenance cost by more than 30% for an aircraft fleet.*” According to IATA, the current maintenance cost varies between \$418 and \$17,533 (with an avg. of \$3,021) per flight cycle and between \$ 0.5 Mill. and \$ 9.0 Mill. (with an avg. of \$ 3.1 Mill.) per aircraft [3]. NDT techniques for application in SHM should be able to detect any critical changes due to damage, both in local and global properties. The Lamb wave method is very promising for SHM due to its long-range capability, and therefore has a high potential for SHM of aging aircraft structures. [2]

Several researchers have studied the implementation of SHM in aging aircraft have been performed. Zagrai and Giurgiutiu developed an electro-mechanical impedance method for damage detection in thin circular plates. [4] Strategies for SHM implementation in aircraft life extension were studied by Kapoor et al. [5] in order to demonstrate the potential economic benefit of SHM in aging aircraft. Two larger EU-FP6 and FP7 projects, called AISHA and AISHA-II [6], respectively, achieved promising results, such as the detection of corrosive and hydraulic liquids based on the collapse of percolation conductivity. [7] Ikegami and Haugse [8] discussed the end-user requirements for an effective SHM system for aging fleets including the sensor systems for characterizing the health of the structure, data interpretation method and signal processing.

Despite this, many challenges remain. One of them is the varying damage size in a large complex structure. In experimental work, an analysis of this is limited due to the prototype cost. To overcome this, a simulation can be made. Many researches simulated Lamb wave propagation by using the finite difference method, finite integration technique, or finite and spectral element method. [9-12] However, the efficiency of the developed models in performing such calculations in large structures is still limited.

The goal of this research is therefore split in three key areas. Firstly, to model a cut fuselage section and to optimize the model itself by “tweaking” several simulation parameters. Secondly, to understand the interaction of Lamb wave with geometrical complexity introduced by the tolerated damage. Thirdly, to study and characterize possible actuator/sensor network configurations in order to enable the reliable detection of the tolerated damage.

2. Theory and Research Methodologies

2.1. Damage Tolerance on Primary Aircraft Structures

The definition of damage tolerance according to Schijve [13] is “*the ability of the structure to sustain anticipated loads in the presence of fatigue, corrosion or accidental damage until such damage is detected through inspections or malfunctions and is repaired*”. In practice, the tolerable damage size in aircraft structures ranges from “*a few millimeters up to a meter or more*”, depending on the initial crack location. [1] The project will focus on a damage tolerant fuselage panel from the main door frame of a Gulfstream G650, as depicted in Fig.1 (red rectangle) and Fig. 2.

2.2. 3D-Model of the Concerned Structure

A 3D model of the fuselage section was created on the CATIA V5 platform. Due to complexities in the fuselage such as rivet holes, large holes for Pitot tube, stringers, curvature, and step thickness, a model simplification was created by extracting those complexities in a single CATProduct. The stringer itself is made of Al2024-T3 and this alloy is known to have significant crack retardation effect [14] in comparison with the doubler material (Al7075-T6). This lowers the probability of damage and therefore the stringer was not modelled in this project.

Assuming that the layers are perfectly bonded and due to very similar acoustic properties, the panel is modelled with Al7075-T6 properties. The extracted complexities are distributed in four sub-

panels; three of them are presented in Fig. 3a-c. In each sub-panel, a half-crack with length “a” propagating from both sides of a hole is introduced. According to Barlow’s formula, the hoop stress for a thin-walled cylinder is twice larger than the axial stress. Logically, the horizontal crack has more probability to appear than a vertical crack and therefore, the project is focused on a horizontally propagating crack.



Fig. 1: Relevant Fuselage Area of G650 for the Project [15]

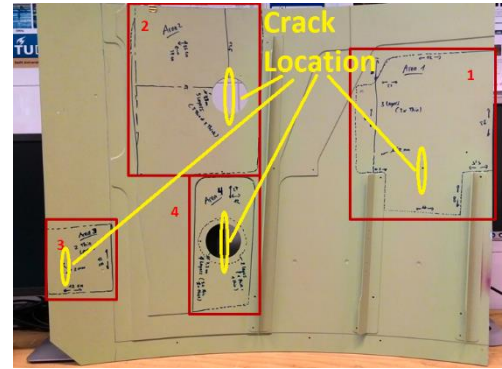


Fig. 2: Cut Fuselage Panel

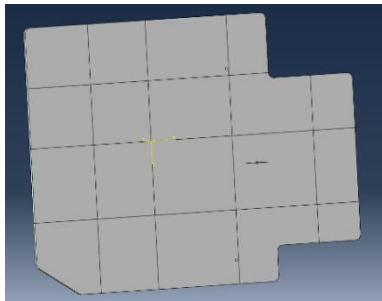


Fig. 3a: Sub-Panel 1
2.77 mm thick with 3 Rivet holes

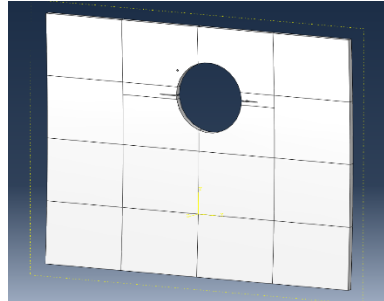


Fig. 3b: Sub-Panel 2
5.96 mm thick with Curvature & Pitot hole

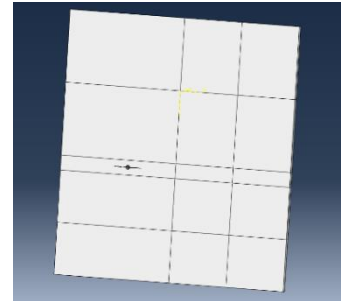


Fig. 3c: Sub-Panel 3
1.96 mm thick with Rivet hole

2.3. Lamb Wave and Dispersion Curve

The theory of Lamb wave propagation is thoroughly described in [16-20]. The dispersion curves for the phase and group velocity of Lamb wave in Al7075-T6 are depicted in Figs. 4 and 5, respectively. For phase velocity, the maximum allowable cut-off frequency-thickness before A_1 mode appears is approximately 1.8 MHz*mm and the group velocity is approximately 1.7 MHz*mm as marked by green lines in Fig. 4 and 5. To ensure that a higher order Lamb mode does not appear, a constant cut-off frequency of 1.2 MHz*mm will be applied for this study. At this frequency-thickness product, the theoretical group velocities of the S_0 and A_0 modes are 4780 m/s and 3020 m/s respectively.

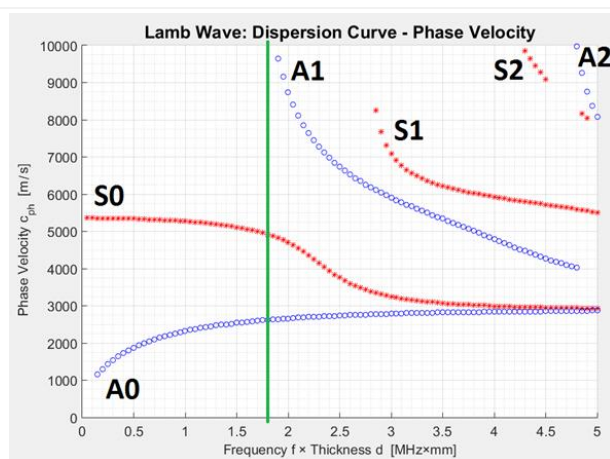


Fig. 4: Phase Velocity Dispersion Curve for Al7075-T6

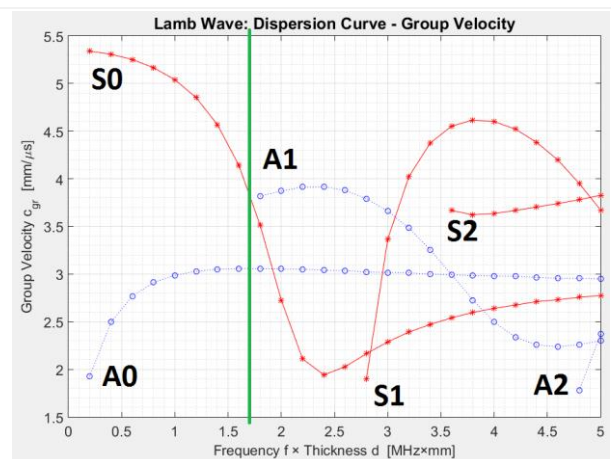


Fig. 5: Group Velocity Dispersion Curve for Al7075-T6

2.4. Minimum Resolvable Distance (MRD)

A dimensionless parameter called minimum resolvable distance (MRD) [19-20] is introduced. A lower MRD index means a better resolution, therefore more suitability for small damage identification. Since sub-panels 1–4 have different thickness, they have different MRD indices and thus have different optimum frequencies. The calculation of the MRD index for a wave travelling distances of 0.1, 0.2, and 0.3 m in sub-panel 1 is presented here as an example (see Fig. 6), and from there, it can be observed that the MRD index of the A_0 mode continuously decreases, while a maximum for the S_0 mode occurs between 450 and 700 kHz. Applying a higher frequency will increase the detectability by the A_0 mode but will also simultaneously deteriorate the S_0 mode detectability. Therefore, a compensation between both modes must be made. For sub-panel 1, a center frequency of 400 kHz will be applied. Further results are presented in Table 1.

2.5. Convergence Study of Finite Element Method

ABAQUS software (Dassault Systèmes) was used by deploying Hilbert-Hughes-Taylor time integration. To determine an optimum mesh size and type, a convergence study was conducted. Four element types were studied: 4 nodes linear tetrahedron (C3D4), 10 nodes quadratic tetrahedron (C3D10), 8 nodes linear hexahedron (C3D8R), and 20 nodes quadratic hexahedron (C3D20R). The detailed methodology of the study is described in [18]. For a large geometry, a trade-off between total computational time and computational error must be made. In Fig. 7, only the quadratic elements C3D10 and C3D20R show a constantly decreasing computational error starting from 2.5 finite elements per A_0 wavelength. The adjusted mesh sizes for other sub-panels are shown in Table 1.

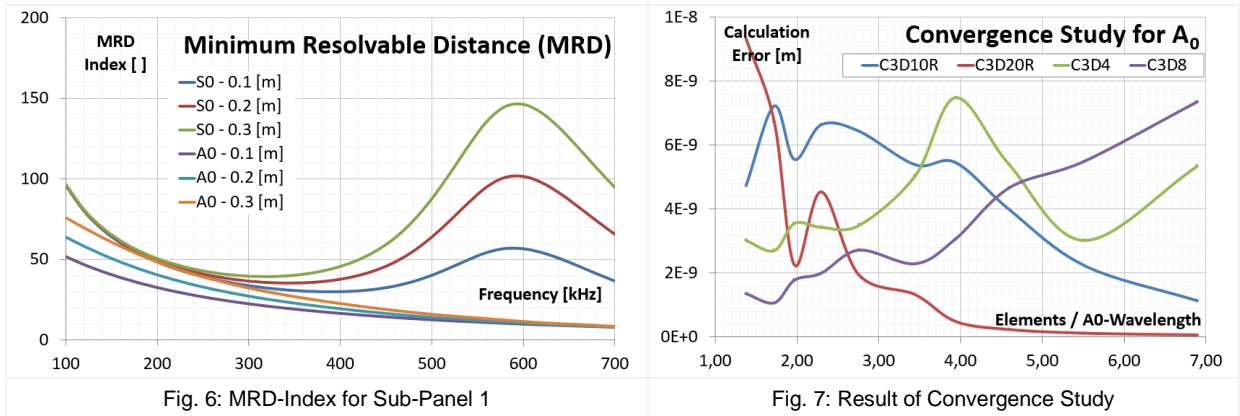


Fig. 6: MRD-Index for Sub-Panel 1

Fig. 7: Result of Convergence Study

2.6. Time Increment Size

The time discretization of equation of motion is needed as well. The minimum requirement to ensure numerical stability of time integration is given by the Courant-Friedrich-Lewy (CFL) condition [11]. The CFL condition stipulates that the wave should not travel more than one element width h in one time increment Δt_{CFL} . For the Newmark time integrator, the recommended time step Δt_{rec} is 20 increments per cycle of the maximum frequency, so that solutions can be calculated in an efficient manner, especially for ultrasounds with frequencies in the MHz [12]. The calculated necessary and recommended time step are listed in Table 1. A uniform time increment of 0.1 μs for all sub-panels was selected, so that an even iteration number can be obtained.

Sub-Panel	Frequency [kHz]	A_0 - λ [mm]	FE size [mm]	No. of FE per A_0 - λ	Δt_{CFL} [μs]	Δt_{rec} [μs]
1	400	6.38	1.50	4.3	0.590	0.125
2	200	12.75	2.00	6.4	0.790	0.250
3	600	4.25	1.00	4.3	0.390	0.083
4	300	8.50	1.25	6.8	0.490	0.166

Table 1: Calculated Minimum FE per A_0 Wavelength and Selected FE Size

2.7. Transducer Placement and Wave Mode Selection

To avoid reflected wave packets and subsequent mode overlapping, the actuators and sensors should not be located near any edges, holes or structural joints, and as clearly separated as possible. If this condition is not fulfilled, signals can overlap (Fig. 9 top). Depending on the crack size and specimen geometry, a certain wave mode can be selected. While the S_0 mode is sensitive to a crack located anywhere inside a plate, the A_0 mode is more sensitive to superficial and subsurface cracks. For a given excitation frequency, the A_0 mode is more efficient for detecting smaller cracks, and visually easier to be tracked during the simulation. For this research, an out-of-plane excitation of 1 N is used to predominantly excite the A_0 mode.

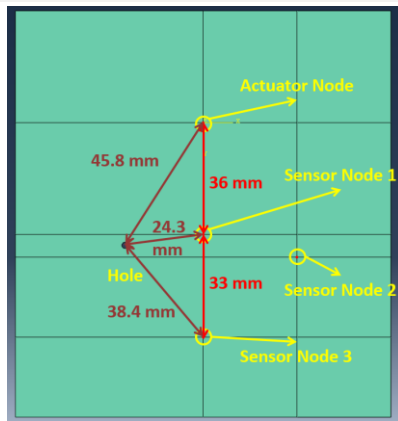


Fig. 8: Sensor Placement of Sub-Panel 3

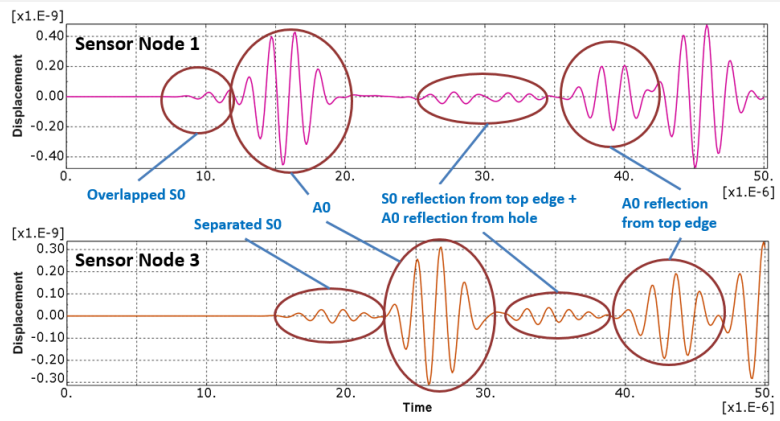


Fig. 9: Signal Obtained from Sensor Node 1 (Top) and 3 (Bottom)

3. Results and Discussion

3.1. Model Verification

An analytical verification is made by calculating the time-of-flight of both the S_0 and A_0 modes. Consider only sub-panel 3 (Fig. 8), which is excited by a 600 kHz 5-cycles Hanning window with a duration of 8.33 μs , as an example for the model verification. The recorded signals at sensor nodes 1 and 3 are shown in Fig. 9 bottom and top, respectively. The theoretical time-of-flight (TOF) for sub-panel 3 at each sensor is calculated by using the shortest wave path between actuator and sensor nodes. The first S_0 and A_0 signals at sensor node 3 (Fig. 9 bottom) are captured at around 15 μs and 22.5 μs , respectively and these are a good match with the theoretical value (14.43 μs and 22.85 μs , respectively). As for sensor node 1 (Fig. 9 top), the first S_0 signal is captured at around 8 μs . However, in this node S_0 overlaps A_0 and it is impossible to determine when the first A_0 signal arrives.

3.2. Signal Interpretation

Here, only the results of sub-panel 1 for the signal interpretation and signal processing (see Section 3.3) will be given. The transducer configuration of sub-panel 1 is depicted in Fig. 11. By using a ray tracing of the shortest propagation distance given in table 2, the location of the crack can be estimated. Both in sensor 1 and 3, the first two arriving modes of the baseline signal do not differ with any scenario because the wave front has not touched the crack tip yet (see Fig. 11). The first remarkable changes appear between 43 μs to 62 μs in node 1 and 48 μs to 65 μs in node 3, respectively. These are the reflected A_0 modes from the crack and they overlap with reflected S_0 modes from both bottom and right edges. At this stage, the original waveform (5 cycles with period of 12.5 μs) cannot be observed anymore. Furthermore, the amplitude differences captured by sensor nodes 2 and 4 are visible right from the beginning of the response, where the first two arriving modes show amplitude differences for each crack length. This happens because the crack is located between the actuator node and sensor nodes 2 and 4. For sensor node 2, the slightly distorted A_0 still maintains its original form at first, however a large portion of amplitude difference can be observed from the center of the wave to its tail (55 μs to 63 μs) due to the increasing wave travelling path.

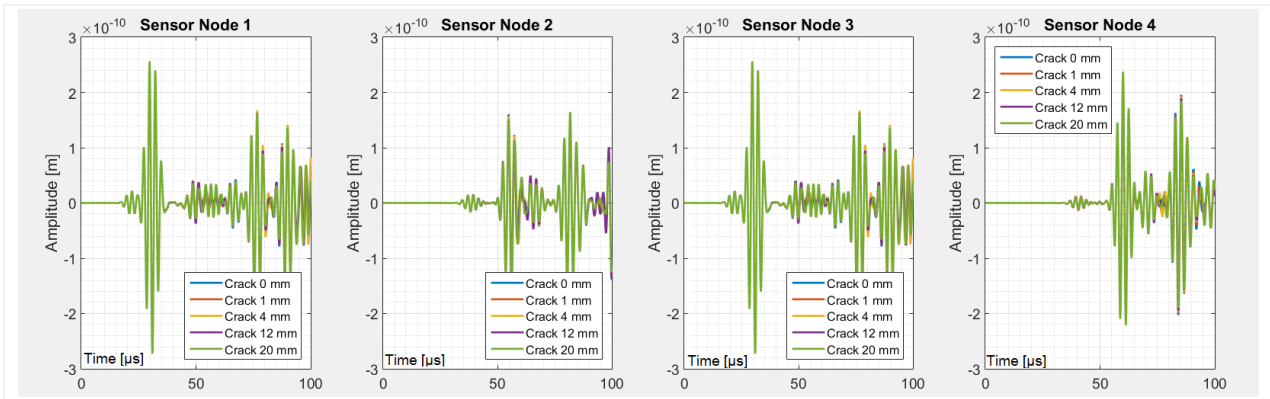


Fig. 10: Received Signal in Sub-Panel 1

3.3. Signal Processing: Time-Domain Signal Subtraction and Hilbert Transform

To highlight the change in amplitude, the signal obtained at each sensor node in the undamaged condition (baseline) can be subtracted from the corresponding signals for each crack scenario. The signal difference is called the residual time-trace. A Hilbert-Transform is applied to obtain the envelope of the residual time-trace, then it is divided by the maximum amplitude of the excitation signal and converted to percentage. The result of each of the sensor nodes is depicted in Fig. 12, which shows that the amplitude change varies between 0.01% to more than 0.2% of the maximum excitation amplitude. Far-away sensor location implies lower detection capability. This result matches perfectly with the MRD formula [20], where l here is the sensor distance. This explains the fact that the adjacent sensors to the crack location (Sensor nodes 1, 2, 3, and 4) have a good detectability and the far-away sensors (Sensor nodes 5, 6, and 7) have a poor detection capability. Logically, the medium distance nodes (8, 9, and 10) have a better detectability than nodes 5, 6, and 7 but lower than sensor nodes 1, 2, 3, and 4.

3.4. Detectability Map

The performance of an SHM system can be measured by quantifying its detection capability or detectability. Statistical criteria can be made by classifying the corresponding normalized subtracted amplitude. An example for this correlation between crack detectability and an amplitude change is given in Table 3. While in Fig. 10 the signal of the 1 mm crack is not presented in order to avoid reading confusion, the detectability map of 1 mm crack will be presented in this section to give the detectability limit of the concerned SHM configuration.

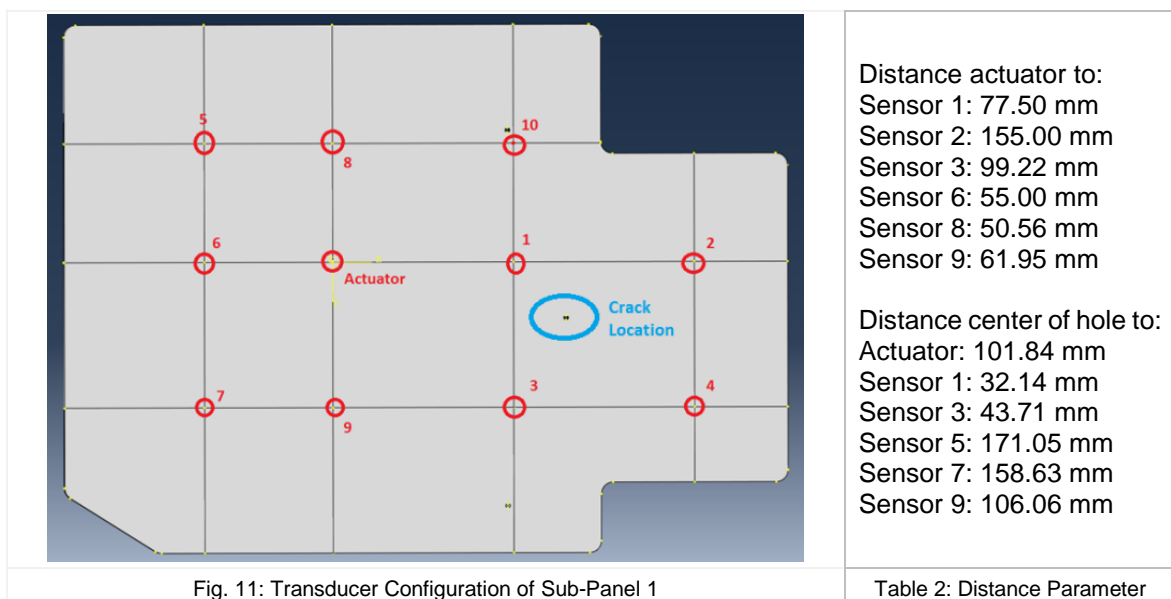


Fig. 11: Transducer Configuration of Sub-Panel 1

Table 2: Distance Parameter

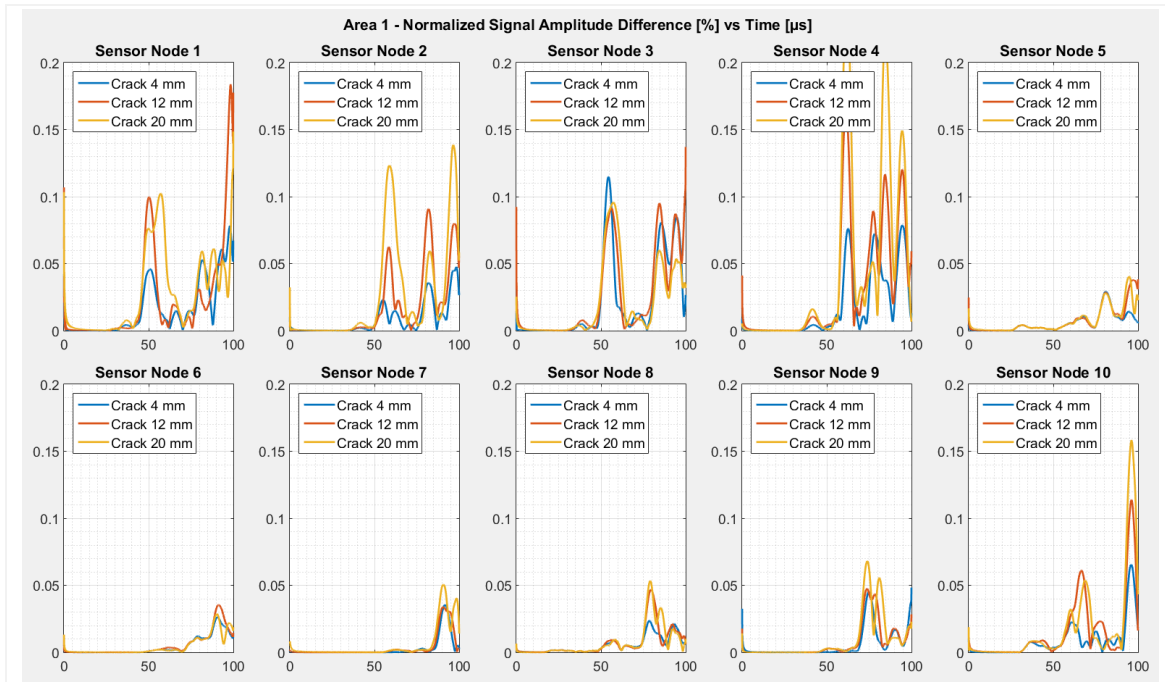


Fig. 12: Subtracted Wave Envelope for Sensors in Sub-Panel 1

Amplitude Change	Classification	Color Code
< 0.02%	Bad	Red
0.02% – 0.04%	Poor	Purple
0.04% – 0.06%	Medium	Orange
0.06% – 0.08%	Good	Green
>0.08%	Excellent	Blue

Table 3: Detectability Quantification

By applying the threshold levels presented in Table 3, an approximate crack detectability map of sub-panel 1 with selected sensor nodes can be drawn, as depicted in Fig. 13a-d. While adding more sensors to a location under the same coverage will not improve the global detectability, moving or adding a new actuator into a different location could drastically change the detectability.

The reason to choose 0.02% as the lower threshold (instead of null threshold) is to avoid faulty detection which could be caused by environmental noise. In Fig. 13a, it can be seen that the detectability is medium to excellent for almost all sensor nodes, except for nodes 5 and 6, which can only poorly detect the 20 mm crack. While there is no doubt that within the area covered by sensor node 1, 2, 3, 4, and 10 an excellent detectability for medium to large size crack can be guaranteed, the detectability issue becomes more critical when it comes to a smaller crack.



Fig. 13a: Detectability Map for a 20 mm Crack

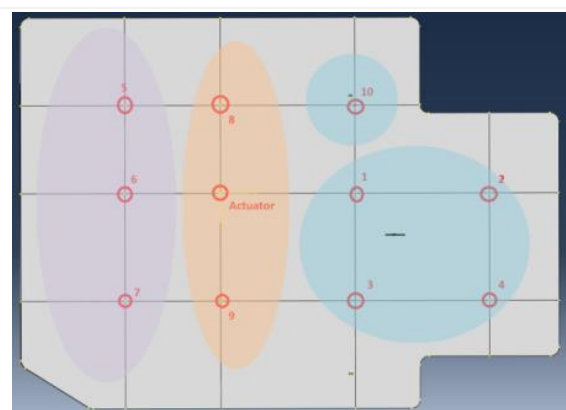


Fig. 13b: Detectability Map for a 12 mm Crack

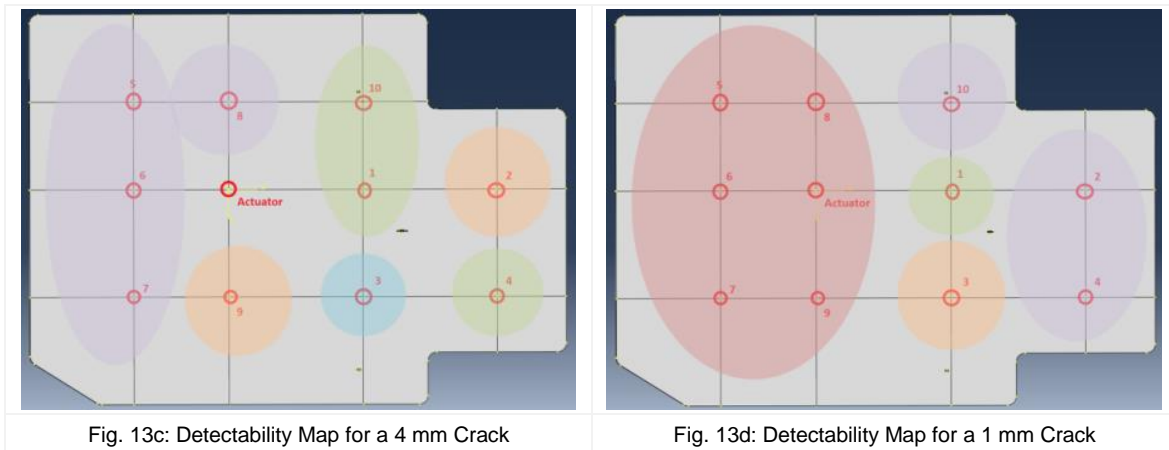


Fig. 13c: Detectability Map for a 4 mm Crack

Fig. 13d: Detectability Map for a 1 mm Crack

4. Conclusion

In this paper, it can be confirmed that a finite element simulation of Lamb wave propagation can provide an estimation about the detectability of the designed SHM system. Despite several simplifications and limitations such as rough mesh size, the numerical results for time-of-flight are in relatively good agreement with the theoretical solution from the dispersion curves for a simple undamaged plate. A minimum size of four FE per A_0 wavelength or higher should be applied to ensure a more accurate simulation, however this must be matched with the computer capabilities and the model specification (geometry, frequency), therefore a trade-off between them is necessary. The result of the detectability map in sub-panel 2 which is presented in the other publication [18] of the first author leads to the conclusion that the curvature effect with radius-thickness ratio of around 200:1 is completely negligible. As stated in [20], the curvature effect of radius-thickness ratio lower than 10:1 must be taken into consideration due to the fact that the group velocity dispersion curve is distorted even in the lower thickness-frequency area.

As a conclusion, it has been shown that with a frequency of 400 kHz excited in a metallic plate of 2.77 mm thickness, a 1 mm crack cannot be detected from a distance of more than 250 mm. To ensure a medium to excellent detection capability of a crack length between 4 and 20 mm, the recommended sensor-crack tip distance should be lower than 200 mm. To further increase the detectability, either the actuator should be moved, or a new actuator must be added. Consequently, a crack with the same size but different direction (e.g. vertical instead of horizontal) requires another sensor placement. Thus, for a limited number of sensors, a specific sensor placement can be good to detect more than one crack type. As a recommendation for future work, SHM should work closely with quality control in product manufacturing to estimate the most probable location for the expected damage to appear.

ACKNOWLEDGEMENT

Special thanks go to Fokker Aerostructures who provided the specimen and J. Kaspar from University of Saarland, Germany, who provided the MATLAB Code for the dispersion curve. The project was funded by the Erich-Becker-Stiftung, a foundation of Frankfurt International Airport.

REFERENCES

- [1]. Boller C. *Why SHM? A Motivation*, in: NATO Lecture Series STO-MP-AVT-220 Structural Health Monitoring of Military Vehicles, Edition: STO Educational Notes (2014).
- [2]. Ochôa P, Infante V, Silva JM, Groves RM. *Detection of multiple low-energy impact damage in composite plates using Lamb wave techniques*. Composites Part B (2015), 80:291-298
- [3]. *Airline Maintenance Cost Executive Commentary – January 2011*. International Air Transport Association. Published by: IATA (2011).
- [4]. Zagrai AN, Giurgiutiu V. *Electro-Mechanical Impedance Method for Crack Detection in Thin Plates*. Journal of Intelligent Material Systems and Structures (2001). 12:709-718

- [5]. Kapoor H, Boller C, Giljohann S, Braun C. *Strategies for Structural Health Monitoring Implementation Potential Assessment in Aircraft Operational Life Extension Considerations*. Proc. 2nd Int. Symp. NDT in Aerospace, Hamburg (2010).
- [6]. Pfeiffer H, Wevers M. *Aircraft Integrated Structural Health Assessment – Structural Health Monitoring and its Implementation within the European Project AISHA*. EU Project Meeting on Aircraft Integrated Structural Health Assessment (AISHA), Leuven (2007).
- [7]. Pfeiffer H, Heer P, Wevers M. *Project Overview AISHA-II and Detection of Corrosive and Hydraulic Liquids by Gauges Based On the Collapse of Percolation Conductivity*. Proc. 8th Int. Workshop Structural Health Monitoring, Stanford (2011).
- [8]. Ikegami R, Haugse ED. *Structural Health Management for Aging Aircraft*. Proc. SPIE Industrial and Commercial Applications of Smart Structures Technologies (2001). 4332:60-67.
- [9]. Yadav VB, Pramila T, Raghuram V, Kishore NN. *A Finite-Difference Simulation of Ultrasonic Lamb Waves in Metal Sheets with Experimental Verification*. 12th Asia-Pacific Conference on NDT, Auckland (2006).
- [10]. Ambrozinski L, Packo P, Stepinski T, Uhl T. *Ultrasonic Guided Waves Based Method for SHM Simulations and An Experimental Test*. Proc. 5th World Conference on Structural Control and Monitoring, Tokyo (2010).
- [11]. Duzek S, Joulaian M, Düster A, Gabbert U. *Numerical Analysis of Lamb Waves Using the Finite and Spectral Cell Methods*. International Journal for Numerical Methods in Engineering (2014), 99:26-53.
- [12]. Cerniglia D, Pantano A, Montinaro N. *3D Simulations and Experiments of Guided Wave Propagation in Adhesively Bonded Multi-Layered Structures*. Journal of NDT & E International (2010), 43:527–535.
- [13]. Schijve J. *Fatigue of Structures and Materials*. Kluwer Academic Publishers, New York / Boston / Dordrecht / London / Moscow (2004).
- [14]. Celik CE, Vardar O, Kalanderoglu V. *Comparison of Retardation Behaviour of 2024-T3 and 7075-T6 Al Alloys*. Fatigue & Fracture of Engineering Materials & Structure (2004), 27:713-722
- [15]. Pictures and specification of Gulfstream G650, Gulfstream website: <http://www.gulfstream.com/aircraft/gulfstream-g650>. (Last accessed: 27/08/2015)
- [16]. Su Z, Ye L, and Ye L. *Guided Lamb Waves for Identification of Damage in Composite Structures: A review*. Journal of Sound and Vibration (2006), 295:753-780.
- [17]. Ochôa P. *Detection of Multiple Low-Energy Impact Damage in Composite Plates Using Lamb Wave Techniques*. Master's Thesis, Delft University of Technology, Delft / Instituto Superior Técnico, Lisboa (2011).
- [18]. Ewald V. *Post-Design Damage Tolerance Enhancement of Primary Aircraft Structures by Ultrasonic Lamb Wave Based Structural Health Monitoring (SHM) System*. Master's Thesis, University of Saarland, Saarbrücken / Delft University of Technology, Delft (2015).
- [19]. Su Z, Ye L. *Identification of Damage Using Lamb Waves. From Fundamentals to Applications*. Springer-Verlag, Berlin / Heidelberg (2009).
- [20]. Wilcox PD. *Lamb Wave Inspection of Large Structures Using Permanently Attached Transducers*. PhD Thesis, Imperial College of Science, Technology and Medicine, London (2004).
- [21]. Giurgiutiu V. *Structural Health Monitoring with Piezoelectric Wafer Active Sensor*. Academic Press-Elsevier, San Diego, USA (2014).
- [22]. Farrar CR, Worden K. *An Introduction to Structural Health Monitoring, in: New Trends in Vibration Based Structural Health Monitoring*. Springer Verlag, Wien / New York (2010).